Accepted manuscript doi:
10.1680/jgeot.21.00318

Submitted: 05 October 2021

Published online in 'accepted manuscript' format: 14 July 2022

Manuscript title: Correlative neutron and X-ray tomography imaging of pile installation in chalk

Authors: Fernando Alvarez-Borges*, Genoveva Burca†, Robert Atwood*, Andrew James*, Mark Wolstenholme‡ and Sharif Ahmed*

Affiliations: *Faculty of Engineering and Physical Sciences, University of Southampton, formerly Diamond Light Source Ltd., Didcot, UK; †ISIS Pulsed Neutron and Muon Source, STFC, UKRI, Rutherford Appleton Laboratory and Visiting Academic, Faculty of Science and Engineering, The University of Manchester, Manchester, UK and ‡Labman Automation Ltd., Middlesbrough, UK, formerly Diamond Light Source Ltd., Didcot, UK

Corresponding author: Fernando Alvarez-Borges, μ-VIS X-ray Imaging Centre, Faculty of Engineering and Physical Sciences, University of Southampton, University Road, Southampton SO17 1BJ, UK.

E-mail: fjab1m20@soton.ac.uk

Accepted manuscript doi:
10.1680/jgeot.21.00318

Abstract

Neutron and X-ray tomography (NCT and XCT, respectively) are imaging techniques increasingly being applied in geomechanics research. They are used to non-destructively reveal different microstructural aspects of geomaterials: XCT is often used to observe/quantify differences in density or porosity, while NCT reveals the presence and distribution of hydrogenous materials such as water. The correlated use of NCT and XCT for geomechanics and geotechnics research is in its infancy. To this date, very few experiments have been carried out that combine both techniques, and none have been used to investigate geomaterial-structure interaction. This paper presents the first correlative NCT-XCT imaging study of pile installation. A scaled model pile was installed in an unsaturated intact chalk cylinder and in-situ NCT and ex-situ XCT synchrotron-based imaging was applied consecutively. Chalk was used because the behaviour of displacement piles installed in this material is still subject to considerable uncertainty. Results reveal for the first time the interaction between installation-induced changes in chalk density and water distribution variations, with evidence of water displacement into the densified material in the vicinity of the installed pile. A straightforward method for correlative bulk density-moisture content determination from NCT-XCT images of geomaterials are presented and their limitations discussed.

Keywords: Chalk; micro-CT tomography; soil/structure interaction; piles & piling

Accepted manuscript doi:
10.1680/jgeot.21.00318

Introduction

Steel piles are often driven into the Chalk formations of northern and north-western Europe to support various types of buildings. They are extensively used as foundations for offshore wind power infrastructure (see e.g. Le et al. (2014), Muir Wood et al. (2015), Mortimore and James (2015) and Geduhn et al. (2018)). Their widespread use has recently led to intensive research interest due to the significant uncertainties pertaining the estimation of their loading capacity, which impacts foundation design, deployment costs and environmental impacts (Kallehave et al., 2015; Kaldellis and Apostolou, 2017; Jardine et al., 2018; Spyroudi, 2021). These uncertainties largely arise from the substantial changes undergone by the highly porous microstructure of chalk, a soft biomicrite, during pile installation (Hobbs and Atkinson, 1993; Lord et al., 2002). Some of these changes have been recently revealed by X-ray computed tomography (XCT) applied to physical models mimicking pile penetration (Alvarez-Borges et al., 2018; Alvarez-Borges et al., 2021). XCT is a non-destructive technique able to map the internal structure of geomaterials in 3D based on their bulk densities. The application of XCT to observe pile penetration mechanisms in other geomaterials such as sands and clays has also gained popularity (see e.g. Paniagua et al. (2013), Silva and Combe (2015) and Doreau-Malioche et al. (2018)).

Neutron computed tomography (NCT) is another non-destructive 3D imaging technique that has relatively recently drawn the attention of geotechnical scientists (Perfect et al., 2014; Tengattini et al., 2021). This technique involves the use of neutrons to produce 3D images of the internal structure of objects. Neutrons are especially sensitive to hydrogenous materials such as water while at the same time being able to penetrate dense matter with ease, something that is often challenging with X-rays. Thus, NCT reveals aspects of the internal structure of geomaterials that are often not accessible with XCT methods, primarily the distribution of pore water.

The combined used of XCT and NCT for geomechanics research has only recently began to be explored in depth (see e.g. Kim et al. (2013), Stavropoulou et al. (2020) and Syed et al. (2021)). These works have demonstrated that the combined techniques deliver valuable information on the characteristics and behaviour of unsaturated materials. However, their use is yet to become extended. A significant constraint is the very limited availability of facilities that can perform both XCT and NCT imaging (Kaestner et al., 2016; LaManna et al., 2017; Tengattini et al., 2020). Thus, while some initial correlative XCT-NCT scanning for geomechanics and geotechnics research has been carried out in the last few years, this technique has not yet been applied to investigate pile penetration processes in geomaterials, to the authors' knowledge. The present paper aims to set precedence on this matter by presenting an investigation of pile penetration in unsaturated chalk using both NCT and XCT applied to physical models. The specific objectives of this research were (1) compare neutron imaging-based pore water content inferences with X-ray imaging-based bulk density estimations, and (2) observe and measure the effect of pile installation on water content and bulk density measurements.

NCT and XCT imaging was carried out at synchrotron facilities hosted by the Rutherford Appleton Laboratory (RAL) in Oxfordshire, United Kingdom. While RAL benefits from the synchrotron-driven high-resolution and high flux capabilities of these facilities, and from their close proximity, simultaneous synchrotron-based NCT and XCT scanning is not currently possible (anywhere in the world). Instead, NCT imaging of pile installation was carried out in-situ, whereas XCT scanning was performed ex-situ (i.e., the sample was moved from one facility to the other). The size of the physical model, confinement conditions, pile materials and penetration rate were chosen to suit experimental and imaging conditions and

Accepted manuscript doi:
10.1680/jgeot.21.00318

were not intended to be consistent representations of full-size pile installation. Rather, the models reflected basic pile penetration mechanisms in chalk that could be studied using correlative NCT-XCT imaging.

Materials and methods

The experiment consisted in carrying out in-situ NCT scans before and after the installation of a solid, flat-tipped stainless steel model pile into a partially saturated intact chalk cylinder, followed by ex-situ XCT imaging of the sample with the embedded pile. Microstructural features and changes in the water content and density of the chalk sample induced by pile installation were then analysed via the correlation of NCT and XCT images.

Experimental set-up

Sample characteristics

An intact chalk block was collected at a quarry near St. Nicholas-at-Wade in Kent, in southeast England. Site descriptions are available in Buckley (2018) and Alvarez-Borges (2019). The block was cut from the Seaford Chalk formation, which exhibits an average calcite ($CaCO_3$) content of about 98% (Hancock, 1975). The measured average intact dry density was 1.57 Mg/m^3, the specific gravity was assumed to be 2.70 (after Lord et al. (2002)), and the estimated porosity was 42%. The chalk block was saturated by immersion into deionised water infused with chalk powder.

A cylindrical sample was sculpted out of the intact block using a soil lathe. The sample measured 34.90 mm in diameter and about 100 mm in height. Figure 1 depicts a typical sample after sculpting. After sculpting, the sample was placed inside an aluminium tube with an internal diameter of 35 mm and wall thickness of 2.5 mm. The sample was oven-dried at 105 °C before scanning. 4 ml of water were added to the top surface of the sample prior to pile installation, to attain unsaturated wet conditions. Uniformly distributed, 4 ml of water would have theoretically occupied about 10% of the sample pore space. In practice, variable saturation levels were anticipated throughout the specimen.

Test rig and pile installation

The pile installation rig was designed and manufactured in-house. The rig allowed the installation of the 3 mm diameter pile without removing the sample from the tomography stage. The rig featured a linear actuator controlled by a Raspberry Pi® microcomputer, a load cell, and a reaction frame. The pile was attached to a cylindrical pile cap which fitted into the sample tube and guided the vertical movement of the pile. An additional pile-guiding sleeve placed on top of the specimen was used to ensure pile verticality. Both the top cap and guiding sleeve featured off-centred air-release orifices. All rig elements are shown in Figure 2.

Pile installation was carried out by advancing the actuator stem downwards onto the pile cap, thus pushing the pile into the chalk specimen. Actuator displacement was controlled using an in-built potentiometer, which achieved a penetration rate of about 8 mm/min. The pile was installed in a single monotonic push until reaching a tip depth of approximately 30 mm. Figure 3 presents the measured loads at the pile head during installation.

Tomography imaging

Neutron and X-ray tomography scanning involves the exposure of an object to a neutron or X-ray beam to acquire projections (i.e., radiographs) from different angular positions around a vertical axis, termed centre of rotation (COR). For synchrotron-based imaging, samples and experimental set-ups are mounted on a rotating stage while the beam remains stationary. Projection greyscale values are a measure of the beam attenuation properties of the object,

Accepted manuscript doi:
10.1680/jgeot.21.00318

that is, on its ability to absorb or scatter X-ray photons or neutrons. Attenuation is quantified as the reduction in beam intensity (I_t) as it traverses the sample. For monochromatic beams, attenuation is controlled by the incident beam intensity (I_0), the attenuation coefficient of the sample material (μ) and the sample thickness (t). It is described by Beer-Lambert's Law as:

$$I_t = I_0 \exp(-\mu t) \quad \textbf{(1)}$$

Where I_0 is the beam intensity as it reaches the surface of the sample, and μ varies with the elemental composition of the sample material. Thus, projections contain information on both the sample geometry (i.e., its thickness) and chemical composition.

Water content estimation from neutron imaging

Neutron attenuation during imaging largely results from the interactions of these particles with the nuclei of the atoms that form the sample. Thus, neutron attenuation is related to the nuclear cross-section area (and the probability of the neutron interacting with it). Consequently, the neutron attenuation coefficient is usually referred to as the macroscopic cross-section and is typically denoted by Σ instead of μ. Semantic segmentation methods for the quantification of water-filled pore volume in geomaterials are not widely used, as most NCT imaging set-ups cannot resolve on individual soil and rock pores (unless the sample grain size is substantially larger than the detector resolution; see e.g. Kim et al. (2013)). Instead, water content is often derived from Σ values for both NCT and neutron radiography, as described below.

From projection-space pixel grey values

Neutron imaging-derived volumetric moisture content (θ) in geomaterials is usually computed from radiographs or projections (see e.g., Hassanein et al. (2006) and Cheng et al. (2012)). This is perhaps due to the relatively straightforward procedure by which sample water volumes can be derived from projection space using equation (1). From this equation, transmitted intensity measurements may be computed from projections of wet geomaterials (I_{t_wet}) as:

$$I_{t\_wet} = I_0 \exp[-(\Sigma_s t_s + \Sigma_w t_w)] \quad \textbf{(2)}$$

where $\Sigma_s t_s$ and $\Sigma_w t_w$ are the product of macroscopic cross-section and thickness of the solid and water fractions within the sample, respectively. If the same specimen is scanned in dry condition (I_{t_dry}), it follows that:

$$I_{t\_dry} = I_0 \exp(-\Sigma_s t_s) \quad \textbf{(3)}$$

The normalisation of the projections of the wet sample by those of the dry sample results in:

$$-\ln(I_{t\_wet}/I_{t\_dry}) = \Sigma_w t_w \quad \textbf{(4)}$$

where the theoretical Σ_w corresponding to the 2.6 Å neutron beam used in this study amounts to 0.565 mm^{-1}, approximately (NIST, 2021). Thus, θ is defined from neutron projection grey values as:

$$\theta(\%) = \frac{-\ln(I_{t\_wet}/I_{t\_dry})}{\Sigma_w t} \times 100 \quad \textbf{(5)}$$

by recalling that t is the total sample thickness traversed by the beam. In the present study, t varies along the horizontal width of the cylindrical chalk sample as $t = 2(r^2 - a^2)^{0.5}$, where r is the radius of the sample and a is the distance from the sample centreline.

Accepted manuscript doi:
10.1680/jgeot.21.00318

From reconstructed voxel grey values

Moisture content estimations from reconstructed voxel grey values (GVs) of NCT images is less frequent in the literature than projection-based calculations. This is possibly because, unlike projection pixel values, the Σ values represented by voxel greyscale tones do not provide directly accessible information on the proportion of water and solids contained within the voxel volume, and can be affected by the reconstruction method employed. Instead, researchers use Σ/Σ_w as a measure of water saturation (S_w) for each voxel, by assuming that $\Sigma/\Sigma_w \rightarrow 1$ would indicate that the entire voxel volume was occupied by water during imaging, whereas $\Sigma/\Sigma_w \rightarrow 0$ would mean that the voxel volume was completely dry (see e.g., Solymar et al. (2003) and Kim et al. (2012)). Thus:

$$S_w(\%) = \frac{\Sigma}{\Sigma_w} \times 100 \qquad \textbf{(6)}$$

Naturally, this method assumes that the neutron attenuation contribution of the solid and air fractions of the sample is negligible, which is reasonable for highly porous geomaterials with low neutron-attenuation properties (Pleinert et al., 1998). For the present case, Σ_w is about 13 and 140 times larger than the macroscopic cross-section of calcite ($\Sigma = 0.0408$ mm^{-1}; NIST (2021)) and aluminium ($\Sigma \approx 0.004$ mm^{-1}; NIST (2021)), respectively, and several orders of magnitude larger than that of air ($\Sigma \approx 0.0001$ mm^{-1} for N_2, of which air is mostly composed of; NIST (2021)). Considering the volumetric proportions of each material, the NCT-based S_w overestimation is anticipated to be less than 4% for intact chalk regions. This value rises to about 5.5% for the hypothetical scenario where the entire sample was composed by calcite without any air present. A similar conclusion was reached by Kim et al. (2012) pertaining silica sand samples.

Density estimation from X-ray imaging

In contrast with neutrons, X-rays mostly interact with the electron clouds of the atoms that form the sample. Thus, for monoenergetic X-rays, attenuation is approximately linearly correlated with the mean effective atomic number of the imaged object. This allows for a relatively straightforward link between attenuation and bulk density. This is commonly done by correlating the reconstructed GVs of certain materials or regions of the digital volume with their known gravimetric bulk densities (see e.g. Mull (1984), Phillips and Lannutti (1997)). A similar approach is taken here, where the reconstructed GVs of air, intact dry chalk, the aluminium sample tube, and the steel pile were paired with their measured densities, as presented in Figure 4. A calibration function was then derived, shown in this Figure, and applied to all GVs in the reconstructed data to obtain 3D representations of sample bulk density (ρ).

Neutron and X-ray tomography scanning and reconstruction

NCT scans were carried out using the IMAT instrument of the ISIS Neutron and Muon Source (Burca et al., 2018). 1193 projections were acquired throughout 360° of sample rotation, using a 40 mm pinhole aperture, a collimation ratio (L/D) of 250 and a polychromatic quasi-parallel neutron beam with a peak flux wavelength of 2.61 Å within a range of 0.7-7 Å. The exposure time per projection was 30 s using an Andor Zyla 4.2 PLUS sCMOS camera coupled with a LiF/ZnS scintillator and a focussing lens. The pixel size was 55 μm with a field of view (FOV) of approximately 112 mm x 112 mm, which allowed to image the entire chalk specimen in each projection.

Synchrotron XCT imaging was carried out at Diamond Light Source using beamline I12. Projections were acquired using a monochromatic quasi-parallel X-ray beam at 100 keV and synchrotron ring current of 300 mA. A total of 1800 projections were recorded throughout 180° of sample rotation, for each scan, with an exposure time of 0.013 s per projection. The detector system consisted of a PCO.edge 5.5 sCMOS camera equipped with an optics module and scintillator, as described by Drakopoulos et al. (2015) (see also Diamond (2021)). The imaging set-up used achieved a pixel size of 18.5 μm with a maximum FOV of 46 mm wide by 12 mm high. Thus, a total of seven vertically overlapping scans were acquired to cover the region of the sample in which the model pile was embedded. These scans were then digitally stitched after reconstruction.

Tomographic reconstruction involves the generation of a 3D image of the sample from the acquired angular projections. This is usually done using a filtered back-projection (FBP) algorithm based on the application of the inverse Radon transform to sinograms computed from projection images, as explained by, e.g., Hsieh (2015). The process returns an image that it is essentially a 3D array of greyscale values contained in units called voxels. Theoretically, each voxel GV is an uncalibrated measure of the amount of attenuation at its location (i.e., μ or Σ). While projection pixel GVs represent the accumulated attenuation along the thickness of the sample in the path of the beam (i.e., I_t), voxel GVs provide no explicit information about the sample geometry per se.

In the present study, tomographic reconstruction was carried out using Savu (Wadeson and Basham, 2016) by implementing a processing pipeline that included zinger/speckle removal (Atwood et al., 2015), ring artefact suppression (Vo et al., 2018), automated COR determination (Vo et al., 2014) and FBP reconstruction (Ramachandran and Lakshminarayanan, 1971; van Aarle et al., 2016). A phase contrast step based on Paganin et al. (2002) was added for reconstructions used solely for 3D visualisation (see Section 3).

It should be noted that reconstructed computed tomography volumes reflect average conditions between the start and end of the scan. Features that change or move during scanning, like pore water in the present experiments, may therefore exhibit different amounts of blurring in the reconstructed volumes depending on the magnitude of the change between the start and end of the scan.

Results and discussion

Figure 5 presents neutron radiographs of the chalk sample in dry condition (a), after wetting (b) and after pile installation, halfway through the NCT scan (c). The addition of water and the installation of the model pile clearly resulted in a reduction of the transmitted intensity, as anticipated from the neutron attenuation properties of water and steel. These radiographs evidence that water continued to seep into the sample during pile installation and NCT acquisition. A projection-based animation of water seepage into the chalk sample prior to pile installation is available in the supplementary material ('water_infiltration.gif').

3D views of the reconstructed NCT and XCT data are given in Figure 6. These images were rendered in Avizo Lite© using the same rendering method and greyscale range to demonstrate the differences emerging from the application of each scanning technique. Orthogonal XY (horizontal) slices are included to aid perspective. Greater neutron and X-ray attenuation is represented by an increase in voxel GV, that is, an increment in brightness. Thus, this Figure highlights different features depending on the imaging method. For instance, the chalk sample in the NCT image shown in Figure 6b becomes progressively darker towards the bottom, as pore water presence and neutron attenuation decreased with sample depth (from the top horizontal surface). It is also brighter than the 3D image for the same material shown in Figure 6a, due to the dry state and much lower neutron attenuation

properties of the latter. In contrast, the XCT volume in Figure 6c shows fairly constant GVs across the chalk specimen. Exceptions are microstructural features such as the bright diagonal streaks, bright regions close to the pile, and a dark streak network near the top of the sample (also visible in Figure 6b). Brighter regions of are indicative of higher bulk densities, while the dark streaks correspond to open fractures (i.e., very low-density zones). Both are discussed later in Sections 3.1 and 3.2, respectively.

1.1. Water and bulk density distribution

Water content distribution in projection space was calculated as described in Section 2.3.1 and results are presented in Figure 7. As discussed previously, it may be noted that the waterfront continued to advance downwards through the pore network during NCT scanning due to gravity, moving from a vertical depth of about 30 mm to 32 mm in 113 minutes (at the start of the NCT scan). Gaps between the chalk sample and the confinement tube favoured water seepage, as may be seen from the higher moisture contents close to lateral boundaries of both contour maps.

Figure 8 presents 3D water saturation and bulk density distribution maps derived as described in Section 2.3.2 and 2.4, respectively. This Figure shows that the water gradient observed in radiographs (in Figure 5 and Figure 7) is reflected in the reconstructed data, albeit in a somewhat less stratified fashion with persistence of higher saturation levels in the periphery of the upper levels of the sample. This further evidence the preferential diffusion through the sample boundaries, and of the blurring effect introduced by the slow downward movement of the waterfront during NCT acquisition, as mentioned in Section 2.5. It is also confirmed in Figure 8 that the pre-existing diagonal bands mentioned previously exhibit higher bulk densities than the surrounding matrix (Figure 8b), and thus resemble natural (pre-existing) compactional features (Mortimore, 1986; Wennberg et al., 2013). However, Figure 8 also shows that these bands exhibit higher local water saturation ratios than adjacent sample areas, a characteristic that is also observed in the dim appearance of these bands in the NCT scan of the dry specimen (Figure 6a) and the subsequent brightening upon wetting (Figure 6b). This is possible evidence of water being lodged in the nano-to-microscopic pore network within these bands (Müter et al., 2014), despite having a lower porosity than the surrounding matrix. Similarly, darker nodules in Figure 6c suggest the presence of porous features, yet they do not seem to have retained a significant amount of water as to become notably brighter in the NCT volume shown of Figure 6b. This inability to retain water is also apparent in the fracture network of the post-installation images in both Figure 6 and Figure 8, where it may be seen that, as with the high porosity nodules, fracture regions exhibit both low bulk density and low saturation ratios. Such behaviour is generally expected of porous geomaterials, as the predisposition of an unsaturated geomaterial matrix to draw water into its pores (matric suction) tends to decrease with increasing porosity/pore size (Mitchell and Soga, 2005).

Effect of pile installation

XCT scan results presented in Figure 6c and Figure 8b show that pile installation produced two major physical changes in the chalk sample: (1) pile insertion led to fracturing of the sample (shown in Figure 6b-c near the top of the sample), and (2) pile penetration crushed the chalk and produced a sleeve-like interface of densified material around the pile shaft, with a noticeable ‘bulb’ or nosecone of dense crushed chalk under the pile tip. Fractures have been attributed in previous research to tensile circumferential stresses mobilised during penetration, which would lead to fracturing when the sample confinement is insufficiently stiff (Alvarez-Borges et al., 2021). Densification (i.e., volumetric deformation) has been identified as possibly the main penetration mechanism for piles in chalk, as the pile volume is

Accepted manuscript doi:
10.1680/jgeot.21.00318

lodged in the material chiefly by the crushing and reduction of pore space of the material in the path of the pile (beneath the advancing pile tip) and in the immediate vicinity (Alvarez-Borges et al., 2018; Buckley et al., 2018; Alvarez-Borges et al., 2021). The formation of a bulb or 'nosecone' of densified material under the pile tip as a key pile penetration mechanism was first identified by White and Bolton (2004) using 2D physical model tests of pile installation in uncemented sand. Previous XCT research involving model piles installed in intact chalk have reached similar conclusions by using laboratory-based polychromatic cone-beam scanners (Alvarez-Borges et al., 2018; Alvarez-Borges et al., 2021). However, Figure 8b showcases penetration-induced density changes in 3D at a level of precision inaccessible by these XCT systems, as the use of wide-spectrum polychromatic X-rays reduces the accuracy of XCT-based density inferences. Additionally, the X-ray flux available at conventional laboratory-based or 'benchtop' XCT systems is orders of magnitude smaller than those produced at modern synchrotron facilities (Brunke et al., 2008), which results in very low X-ray transmission and/or very long scanning times for dense and/or metallic samples, like the one used in the present study. Thus, Figure 8b demonstrates the sharp density gradient towards the pile wall previously proposed by Alvarez-Borges et al. (2021), but with an accuracy not achieved previously, depicting density increments of up to 60% very close to the pile shaft. It should be noted that benchtop XCT scanners are the only technology currently available for fully simultaneous NCT-XCT imaging (Kaestner et al., 2016; LaManna et al., 2017; Tengattini et al., 2020).

NCT images shown in Figures 4–7 provide complementary information on the penetration processes revealed by XCT. For instance, Figure 7 shows that the gravity-driven downward movement of water was affected by pile installation, with a noticeable nosecone feature of moister material forming under the pile tip. Furthermore, Figure 6c and Figure 8a evidence that water presence increased in sample regions densified by pile penetration, i.e. in the vicinity of the pile shaft and under the pile tip. While this may seem counterintuitive at first, the densification of significantly undersaturated soils by mechanical action can result in greater water saturation of the pore volume, as air is preferentially expelled out of pore space, or compressed, and matric suction may increase with decreasing porosity as mentioned before (Mitchell and Soga, 2005; Powrie, 2014). This is routinely observed in standard compaction curves, and contrasts with the general behaviour of saturated geomaterials where densification is directly linked with reductions in moisture content. Additionally, the pore water in the sample region subsequently occupied by the pile can be surmised to have been displaced into the adjacent zones of densified chalk, thus contributing to the measured increased in saturation and moisture content.

A comparison between water content profiles of the vicinity of the pile before and after pile installation, extracted from Figure 7 and presented in Figure 9a, suggest that the expelled water may have continued with the general downward trend, leading to 'drier' conditions in the shallower regions of the densified chalk sleeve, and 'wetter' conditions in deeper zones like under the pile tip. Similarly, horizontal bulk density and water saturation profiles that traverse the nosecone region, provided in Figure 9b (extracted from Figure 8), further support the inference that installation crushed the chalk matrix in the path of the pile and displaced both the crushed material and pore water to create a denser, wetter interface around and beneath the installed pile. A notable implication is that gravimetric moisture content measurements of the pile interface after exhumation, as those performed by, e.g., Buckley et al. (2018), may not be fully accurate indicators of densification if the chalk was not fully saturated prior to pile installation.

Accepted manuscript doi:
10.1680/jgeot.21.00318

Study limitations and outlook

Neutron and X-ray scattering

Neutron and X-ray attenuation processes involve subatomic particle scattering. Scattered particles do not follow the original beam path direction but may still impact on the detector system producing spurious greyscale counts (Hassanein, 2006; Boillat et al., 2018; Vo et al., 2019). This is exemplified for neutrons in Figure 10, which depicts normalised background GV counts along the sampling paths shown in Figure 5. It may be seen that the GV profiles are higher than those of the flatfield image due to the incidence of scattered neutrons onto the detector system. A similar effect occurs with X-rays, as shown by, e.g., Vo et al. (2019). The spurious counts are higher for neutron radiographs taken after wetting the sample and installing the pile, as these conditions favoured greater neutron beam attenuation by scattering. However, the shift in counts is less than 5% of the incident intensity even after wetting and pile installation, and thus, the effect on moisture content measurements may be surmised to be relatively modest for the present study. Comparable results were obtained from X-ray radiographs. This may not be the case in other applications, but hardware- and software-based corrections are available to mitigate this (Boillat et al., 2018; Vo et al., 2019). Post-scan gravimetric calibration of XCT/NCT measurements can also be carried out in future work, though these are often difficult to perform on small samples and the process involves the destruction of the specimen.

The neutron absorption and scattering properties of water also precluded the use of the NCT set-up of this study on fully water-saturated chalk samples, as shown in Figure 11. The very low transmission values in Figure 11a demonstrate that pore water prevented most neutrons from reaching the detector area behind the sample, as similarly observed by Syed et al. (2021). Thus, the use of NCT systems and experimental set-ups similar to those of this investigation may be unsuitable for water-saturated porous soil/rock samples. However, though not yet routinely used in geomechanics, researchers have successfully used deuterated water (heavy water) as an alternative saturating liquid for the NCT imaging of soils, as it has a lower neutron scattering cross-section and similar X-ray attenuation coefficient to that of water (e.g. Kim et al. (2013)). That said, greater errors in water content estimation may occur due to the attenuation properties of deuterated water being much closer to those of the other materials in the sample, as discussed in Section 3.3.2. Alternatively, it may also be possible to further reduce the model size in future work, and thus, the amount of water present at full saturation. However, the preparation of smaller diameter intact specimens and the use of model pile diameters below 3 mm may be impractical.

Material heterogeneity, polychromatism, and beam hardening

In addition to scattering effects, density and water content measurements may have been affected by the composition of the scanned object. Chalk exhibits a heterogeneous microstructure of calcite particles with air- and/or water-filled pore space, as may be inferred from Figure 6c and Figure 8b. For XCT imaging, this heterogeneity suggests that the GVs used to produce the density calibration function may not be considered absolute matches to the extrapolated chalk densities. For the NCT data, the contribution of the of the aluminium sample tube and the steel pile to beam attenuation, as well as the localised densification of the chalk induced by pile installation, may have affected water content computations. That said, the proposed XCT density calibration function is a good linear fit to the correlated data (Figure 4), as expected from Equation (1). Calibration accuracy might be further improved in the future by the use of dedicated calibration phantoms, as often done in medical sciences (e.g., Borah et al. (2005)). For NCT-based water content measurements, the attenuation

contribution of the aluminium cylinder, the steel pile and pure calcite is small compared to that of water ($\Sigma \approx 0.004$ mm^{-1}, $\Sigma \sim 0.12$ mm^{-1}, $\Sigma = 0.0408$ mm^{-1} and $\Sigma_w = 0.565$ mm^{-1} for aluminium, steel, calcite and water, in each case; NIST (2021)), as discussed previously in Section 2.3.2. It may be therefore surmised that the effect of these materials on water content computations were modest (note that this may not be the case when using deuterated water with much lower neutron attenuation properties). However, the changes in neutron attenuation resulting from the redistribution of calcite particles associated with the crushing, remoulding and densification of chalk during pile installation are of particular interest, as these processes occur in regions where water content may have changed as well. This may be investigated by comparing NCT and XCT voxel value data for dry specimen regions containing natural chalk density variations, and assessing how the different in XCT-based density estimations correlate with NCT-based water content inferences. This has been carried out using one XY slice for each volume located at a depth of 36.5 mm below the sample surface (both slices shown in Figure 12(a, b)). This depth is well into the dry zone below the waterfront (see Figure 7). The XCT slice has been digitally binned (3 × 3 pixel bins) to match the dimensions of the NCT slice. A 10 × 10 mm grid containing sampling windows 1 × 1 mm in size has been used to retrieve 100 local average grey values (one per sampling window) at the centre of the slices, as presented in Figure 12(a, b). Figure 12(c) presents the correlation between density and saturation ratios derived from the sampled XCT and NCT grey value data. As expected, higher chalk densities return spuriously higher water saturation values. However, the correlated data suggests that even substantial increases in chalk density, like those estimated for regions close and underneath the pile tip (Figure 8), would result in very modest water saturation overestimations, possibly of up to about 0.10% at the density of pure calcite. A similar correlative assessment could be carried out using a 3D sampling grid, and correction patterns could potentially be derived and applied to water saturation maps for more highly attenuating samples. Nevertheless, great care must be taken when extracting direct empirical correlations between XCT and NCT data, as no linear relationship exists between the X-ray and neutron attenuation properties of different materials (as discussed in Sections 2.3 and 2.4).

The use of a polychromatic beam for NCT imaging lead to the preferential attenuation of lower energy neutrons close to the specimen surface, an effect known as beam hardening (Hsieh, 2015). This artefact produces a gradual decrease in GVs from periphery to the centreline of the reconstructed object, and can lead to the underestimation of water thickness computations for highly-attenuating samples (Kang et al., 2013). However, the effect on low-attenuation samples is generally small (Vontobel et al., 2006), and it is not evident in this study (see e.g., Figure 9b). This agrees with the work of Hussey et al. (2012), who reported limited beam hardening effects for t_w values below ≈5 mm. The chalk sample of this study exhibited localised t_w maxima of about 2 mm.

The use of a polychromatic neutron beam also contravenes Beer-Lambert's law considerations, which assume that the incident beam is monoenergetic. For polychromatic transmission, the value of Σ_w corresponds to the mean of all the wavelengths present in the beam rather than that at a specific wavelength, as assumed in the present study (Kang et al., 2013), which invariably affects water content measurements (Tengattini et al., 2021). While not used in the present study due to the large increments in neutron exposure time required, IMAT also features energy-resolved ('time-of-flight') imaging capabilities where neutron detection for a given wavelength range can be carried out (Ametova et al., 2021). This feature can be used to further improve the accuracy of NCT-based water content measurements in future work involving smaller samples requiring lower exposure times.

Physical model limitations

Physical modelling of pile installation at normal gravity typically demands sample to pile diameter ratios equal or greater than 50 to minimise boundary effects (Schnaid and Houlsby, 1991). In practice, such sample and pile dimensions would be impracticable for XCT-NCT synchrotron imaging, mostly due FOV size limitations and to the significant reduction in transmission associated with scanning larger objects. Thus, it must be recognised that some of the penetration process observed during pile installation in the present experiments (e.g. fractures, pile head loads, extent of chalk crushing and densification) could be linked to boundary effects associated with the model dimensions.

It should be also noted that the transfer of the sample across facilities, even over short distances, may have resulted in sample disturbance. The use of chalk, a geomaterial with natural cementation, and a pile guiding sleeve may have mitigated this, but the use of unbonded granular samples may require additional care.

Conclusions

Pile penetration in unsaturated chalk was studied by way of physical modelling with correlative synchrotron-based neutron and X-ray computed tomography (NCT and XCT, respectively). The combined use of these imaging techniques for this purpose is new to the field. The objective of this investigation was to preliminarily observe, measure, and correlate the changes in volumetric moisture content and bulk density in chalk induced by pile installation. Main outcomes of this research were:

- A straightforward method for estimating density and moisture content from correlative XCT and NCT images of physical models involving fine-grained geomaterials was described. This method can be easily implemented in future research.
- The reconstructed NCT/XCT data and the proposed image analysis method allowed the 3D observation of sample microstructure and its correlation with local moisture content and bulk density values, as well as the variation in these parameters arising from pile penetration.
- XCT results evidenced that model pile penetration in intact chalk samples leads to increases in bulk density, as observed in previous investigations using fully saturated chalk samples and cone-beam XCT systems.
- NCT-based measurements revealed that moisture content increased within sample regions densified by pile penetration. Such behaviour reflected the partially saturated state of the sample, the XCT-inferred reduction in porosity, and the displacement of pore water from the zone occupied by the pile.
- The approach used had some limitations to be considered in future work, namely: (i) neutron attenuation properties of water may preclude the use of fully saturated porous samples; (ii) neutron and X-ray scattering can affect bulk property measurements; (iii) material heterogeneity can also affect bulk property inferences. These limitations may be overcome using deuterated pore water, hardware- and/or software-based correction methods and dedicated calibration phantoms.

Acknowledgements

The authors gratefully acknowledge the Science and Technology Facilities Council (STFC) for access to neutron beamtime at ISIS Neutron and Muon Source (Experiment rb1920746; https://doi.org/10.5286/ISIS.E.RB1920746), IMAT instrument, as well as Diamond Light Source Ltd for the provision of X-ray beamtime at beamline I12 (proposal MG26232-2). The

authors also acknowledge the Diamond Light Source-University of Southampton collaboration agreement (COL0226) which provided access to the UKCRIC National Infrastructure Laboratory (under EPSRC grant no. EP/P013627/1 and support from the UKCRIC Coordination Node, EPSRC grant number EP/R017727/1) for sample preparation and characterisation. The authors are thankful for the support provided by staff at these facilities.

Notation

a	Horizontal distance from vertical centreline of sample
COR	Centre of rotation
FBP	Filtered back-projection
GV	Grey value
I_t	Transmitted intensity
I_{t_wet}	Transmitted intensity for wet sample
I_{t_dry}	Transmitted intensity for dry sample
I_0	Incident intensity
NCT	Neutron computed tomography
r	Sample radius
S_w	Volumetric saturation ratio
t	Total sample thickness
t_s	Thickness of sample solids
t_w	Thickness of sample water
XCT	X-ray computed tomography
θ	Volumetric moisture content
μ	Attenuation coefficient
ρ	Bulk density
Σ	Macroscopic neutron cross-section
Σ_s	Macroscopic neutron cross-section of sample solids
Σ_w	Macroscopic neutron cross-section of sample water

References

Alvarez-Borges F., Ahmed S., Madhusudhan B.N. and Richards D. (2021) Investigation of pile penetration in calcareous soft rock using X-ray computed tomography. International Journal of Physical Modelling in Geotechnics 22(1): 38-52. https://doi.org/10.1680/jphmg.20.00031

Alvarez-Borges F.J., Richards D.J., Clayton C.R.I. and Ahmed S.I. (2018) Application of X-ray computed tomography to investigate pile penetration mechanisms in chalk. In: *Engineering in Chalk, Proceedings of the Chalk 2018 Conference* (Lawrence J., Preene M., Lawrence U. and Buckley R.M. (eds)). ICE Publishing, London, UK, pp. 565-570. https://doi.org/10.1680/eiccf.64072.565

Alvarez-Borges F.J. (2019) *The Shaft Capacity of Small Displacement Piles in Chalk.* PhD Thesis, University of Southampton, Southampton, UK.

Ametova E., Burca G., Chilingaryan S., Fardell G., Jørgensen J.S., Papoutsellis E., Pasca E., Warr R., Turner M., Lionheart W.R.B. and Withers P.J. (2021) Crystalline phase discriminating neutron tomography using advanced reconstruction methods. Journal of Physics D: Applied Physics 54(32): 325502. https://doi.org/10.1088/1361-6463/ac02f9

Atwood R.C., Bodey A.J., Price S.W.T., Basham M. and Drakopoulos M. (2015) A high-throughput system for high-quality tomographic reconstruction of large datasets at Diamond Light Source. Philosophical Transactions of the Royal Society A 373(2043): 2369–2393. https://doi.org/10.1098/rsta.2014.0398

Boillat P., Carminati C., Schmid F., Grünzweig C., Hovind J., Kaestner A., Mannes D., Morgano M., Siegwart M., Trtik P., Vontobel P. and Lehmann E.H. (2018) Chasing quantitative biases in neutron imaging with scintillator-camera detectors: a practical method with black body grids. Optics Express 26(12): 15769-15784. https://doi.org/10.1364/OE.26.015769

Borah B., Ritman E.L., Dufresne T.E., Jorgensen S.M., Liu S., Sacha J., Phipps R.J. and Turner R.T. (2005) The effect of risedronate on bone mineralization as measured by micro-computed tomography with synchrotron radiation: Correlation to histomorphometric indices of turnover. Bone 37(1): 1-9. https://doi.org/10.1016/j.bone.2005.03.017

Brunke O., Brockdorf K., Drews S., Müller B., Donath T., Herzen J. and Beckmann F. (2008) Comparison between x-ray tube-based and synchrotron radiation-based uCT. In: *Proceedings of SPIE 7078, Optical Engineering + Applications*. SPIE, Bellingham, WA, USA. https://do.org/10.1117/12.794789

Buckley R.M. (2018) *The axial behaviour of displacement piles in chalk.* PhD Thesis, Imperial College London, London, UK.

Buckley R.M., Jardine R.J., Kontoe S., Parker D. and Schroeder F.C. (2018) Ageing and cyclic behaviour of axially loaded piles driven in chalk. Géotechnique 68(2): 146-161. https://doi.org/10.1680/jgeot.17.P.012

Burca G., Nagella S., Clark T., Tasev D., Rahman I.A., Garwood R.J., Spencer A.R.T., Turner M.J. and Kelleher J.F. (2018) Exploring the potential of neutron imaging for life sciences on IMAT. Journal of Microscopy 272(3): 242-247. https://doi.org/10.1111/jmi.12761

Cheng C.L., Kang M., Perfect E., Voisin S., Horita J., Bilheux H.Z., Warren J.M., Jacobson D.L. and Hussey D.S. (2012) Average Soil Water Retention Curves Measured by Neutron Radiography. Soil Science Society of America Journal 76(4): 1184-1191. https://doi.org/10.2136/sssaj2011.0313

Diamond (2021) I12 Detectors. See: https://www.diamond.ac.uk/Instruments/Imaging-and-Microscopy/I12/Detectors-at-I12.html [Accessed 15/07/2021]

Doreau-Malioche J., Combe G., Viggiani G. and Toni J.B. (2018) Shaft friction changes for cyclically loaded displacement piles: an X-ray investigation. Géotechnique Letters 8(1): 66-72. https://doi.org/10.1680/jgele.17.00141

Drakopoulos M., Connolley T., Reinhard C., Atwood R., Magdysyuk O., Vo N., Hart M., Connor L., Humphreys B., Howell G., Davies S., Hill T., Wilkin G., Pedersen U., Foster A., De Maio N., Basham M., Yuan F. and Wanelik K. (2015) I12: the Joint Engineering, Environment and Processing (JEEP) beamline at Diamond Light Source. Journal of Synchrotron Radiation 22(3): 828-838. https://doi.org/10.1107/S1600577515003513

Geduhn M., Barbosa P., Dührkop J., Augustesen A.H., Østergaard M.U. and Steenfelt J.S. (2018) Offshore pile load tests in Chalk to support the design of jacket foundations. Proceedings of the Institution of Civil Engineers-Geotechnical Engineering 171(6): 508-517. https://doi.org/10.1680/jgeen.17.00217

Hancock J.M. (1975) The petrology of chalk. Proceedings of the Geologists' Association 86(4): 499-535. https://doi.org/10.1016/S0016-7878(75)80061-7

Hassanein R., Meyer H.O., Carminati A., Estermann M., Lehmann E. and Vontobel P. (2006) Investigation of water imbibition in porous stone by thermal neutron radiography. Journal of Physics D: Applied Physics 39(19): 4284-4291. https://doi.org/10.1088/0022-3727/39/19/023

Hassanein R.K. (2006) *Correction methods for the quantitative evaluation of thermal neutron tomography.* DSc Thesis, Swiss Federal Institute of Technology in Zürich, Zurich, CH. https://doi.org/10.3929/ethz-a-005273682.

Hobbs N.B. and Atkinson M.S. (1993) Compression and tension tests on an open ended tube pile in chalk. Ground Engineering 26(3): 30-34.

Hsieh J. (2015) *Computed Tomography: Principles, Design, Artifacts, and Recent Advances* (3rd Edition), SPIE, Bellingham, WA, USA.

Hussey D.S., Spernjak D., Weber A.Z., Mukundan R., Fairweather J., Brosha E.L., Davey J., Spendelow J.S., Jacobson D.L. and Borup R.L. (2012) Accurate measurement of the through-plane water content of proton-exchange membranes using neutron radiography. Journal of Applied Physics 112(10): 104906. https://doi.org/10.1063/1.4767118

Jardine R.J., Buckley R.M., Kontoe S., Barbosa P. and Schroeder F.C. (2018) Behaviour of piles in driven chalk. In: *Engineering in Chalk, Proceedings of the Chalk 2018 Conference* (Lawrence J., Preene M., Lawrence U. and Buckley R.M. (eds)). ICE Publishing, London, UK, pp. 33-51. https://doi.org/10.1680/eiccf.64072.033

Kaestner A., Mannes D., Hovind J., Boillat P. and Lehmann E. (2016) Combined neutron and X-ray imaging on different length scales. In: *6th Conference on Industrial Computed Tomography (iCT 2016).* NDT.net, Bad Breisig, DE.

Kaldellis J.K. and Apostolou D. (2017) Life cycle energy and carbon footprint of offshore wind energy. Comparison with onshore counterpart. Renewable Energy 108: 72-84. https://doi.org/10.1016/j.renene.2017.02.039

Kallehave D., Byrne B.W., LeBlanc T.C. and Mikkelsen K.K. (2015) Optimization of monopiles for offshore wind turbines. Philosophical Transactions of the Royal Society A 373(2035). https://doi.org/10.1098/rsta.2014.0100

Kang M., Bilheux H.Z., Voisin S., Cheng C.L., Perfect E., Horita J. and Warren J.M. (2013) Water calibration measurements for neutron radiography: Application to water content quantification in porous media. Nuclear Instruments and Methods in Physics Research Section A: Accelerators, Spectrometers, Detectors and Associated Equipment 708: 24-31. https://doi.org/10.1016/j.nima.2012.12.112

Kim F.H., Penumadu D. and Hussey D.S. (2012) Water Distribution Variation in Partially Saturated Granular Materials Using Neutron Imaging. Journal of Geotechnical and Geoenvironmental Engineering 138(2): 147-154. https://doi.org/10.1061/(ASCE)GT.1943-5606.0000583

Kim F.H., Penumadu D., Gregor J., Kardjilov N. and Manke I. (2013) High-Resolution Neutron and X-Ray Imaging of Granular Materials. Journal of Geotechnical and Geoenvironmental Engineering 139(5): 715-723. https://doi.org/10.1061/(ASCE)GT.1943-5606.0000809

LaManna J.M., Hussey D.S., Baltic E. and Jacobson D.L. (2017) Neutron and X-ray Tomography (NeXT) system for simultaneous, dual modality tomography. Review of Scientific Instruments 88(11): 113702. https://doi.org/10.1063/1.4989642

Le T.M.H., Eiksund G.R., Strøm P.J. and Saue M. (2014) Geological and geotechnical characterisation for offshore wind turbine foundations: A case study of the Sheringham Shoal wind farm. Engineering Geology 177: 40-53. https://doi.org/10.1016/j.enggeo.2014.05.005

Lord J.A., Clayton C.R.I. and Mortimore R.N. (2002) *CIRIA Report C 574: Engineering in Chalk*, Construction Industry Research and Information Association (CIRIA), London, UK.

Mitchell J.K. and Soga K. (2005) *Fundamentals of Soil Behavior*, John Wiley & Sons, Inc., Hoboken NJ, USA.

Mortimore R. and James L. (2015) The search for onshore analogues for the offshore Upper Cretaceous Chalk of the North Sea. Proceedings of the Geologists' Association 126(2): 188-210. https://doi.org/10.1016/j.pgeola.2015.01.008

Mortimore R.N. (1986) Stratigraphy of the upper cretaceous white chalk of Sussex. Proceedings of the Geologists' Association 97(2): 97-139. https://doi.org10.1016/s0016-7878(86)80065-7

Muir Wood A., Mackenzie B., Burbury D., Rattley M.J., Clayton C.R.I., Mygind M., Wessel Andersen K., LeBlanc Thilsted C. and Albjerg Liingaard M. (2015) Design of large diameter monopiles in chalk at Westermost Rough offshore wind farm. In: *Frontiers in Offshore Geotechnics III* (Meyer V. (ed)). CRC Press/Balkema, London, UK, 1, pp. 723-728.

Mull R.T. (1984) Mass Estimates by Computed-Tomography - Physical Density from CT Numbers. American Journal of Roentgenology 143(5): 1101-1104. https://doi.org/10.2214/ajr.143.5.1101

Müter D., Sorensen H.O., Jha D., Harti R., Dalby K.N., Suhonen H., Feidenhans'l R., Engstrom F. and Stipp S.L.S. (2014) Resolution dependence of petrophysical parameters derived from X-ray tomography of chalk. Applied Physics Letters 105(4): 0431081-0431085. https://doi.org/10.1063/1.4891965

NIST (2021) Neutron activation and scattering calculator. See: https://www.ncnr.nist.gov/resources/activation/ [Accessed 24/06/2021]

Paganin D., Mayo S.C., Gureyev T.E., Miller P.R. and Wilkins S.W. (2002) Simultaneous phase and amplitude extraction from a single defocused image of a homogeneous object. Journal of Microscopy 206(1): 33-40. https://doi.org/10.1046/j.1365-2818.2002.01010.x

Paniagua P., Andò E., Silva M., Emdal A., Nordal S. and Viggiani G. (2013) Soil deformation around a penetrating cone in silt. Géotechnique Letters 3(4): 185-191. http://doi.org/10.1680/geolett.13.00067

Perfect E., Cheng C.L., Kang M., Bilheux H.Z., Lamanna J.M., Gragg M.J. and Wright D.M. (2014) Neutron imaging of hydrogen-rich fluids in geomaterials and engineered porous media: A review. Earth-Science Reviews 129: 120-135. https://doi.org/10.1016/j.earscirev.2013.11.012

Phillips D.H. and Lannutti J.J. (1997) Measuring physical density with X-ray computed tomography. Ndt & E International 30(6): 339-350. https://doi.org/10.1016/S0963-8695(97)00020-0

Pleinert H., Sadouki H. and Wittmann F.H. (1998) Determination of moisture distributions in porous building materials by neutron transmission analysis. Materials and Structures 31(4): 218-224. https://doi.org/10.1007/BF02480418

Powrie W. (2014) *Soil Mechanics Concepts and Applications*, Taylor & Francis, Boca Raton, FL, USA.

Ramachandran G.N. and Lakshminarayanan A.V. (1971) Three-dimensional reconstruction from radiographs and electron micrographs: application of convolutions instead of Fourier transforms. Proceedings of the National Academy of Sciences 68(9): 2236-2240. https://doi.org/10.1073/pnas.68.9.2236

Schnaid F. and Houlsby G.T. (1991) An assessment of chamber size effects in the calibration of in situ tests in sand. Géotechnique 41(3): 437-445. https://doi.org/10.1680/geot.1991.41.3.437

Silva M. and Combe G. (2015) Soil-pile interaction during pile installation. Observations from x-ray tomography and 3D-DIC. In: *Deformation Characteristics of Geomaterials - Proceedings of the 6th International Symposium* (Rinaldi V.A., Zeballos M.E. and Clariá J.J. (eds)). IOS Press, Amsterdam, NL, pp. 600-607.

Solymar M., Lehmann E., Vontobel P. and Nordlund A. (2003) Relating variations in water saturation of a sandstone sample to pore geometry by neutron tomography and image analysis of thin sections. Bulletin of Engineering Geology and the Environment 62(1): 85-88. https://doi.org/10.1007/s10064-002-0168-z

Spyroudi A. (2021) Carbon footprint of offshore wind farm components. Offshore Renewable Energy Catapult. https://ore.catapult.org.uk/analysisinsight/carbon-footprint-offshore-wind-farm-components/

Stavropoulou E., Andò E., Roubin E., Lenoir N., Tengattini A., Briffaut M. and Bésuelle P. (2020) Dynamics of Water Absorption in Callovo-Oxfordian Claystone Revealed With Multimodal X-Ray and Neutron Tomography. Frontiers in Earth Science 8(6). https://doi.org/10.3389/feart.2020.00006

Syed A., Tanino Y., LaManna J.M., Jacobson D.L., Hussey D.S., Baltic E. and Burca G. (2021) A portable triaxial cell for beamline imaging of rocks under triaxial state of stress. Measurement Science and Technology 32(9): 095403. https://doi.org/10.1088/1361-6501/abeb94

Tengattini A., Lenoir N., Andò E., Giroud B., Atkins D., Beaucour J. and Viggiani G. (2020) NeXT-Grenoble, the Neutron and X-ray tomograph in Grenoble. Nuclear Instruments and Methods in Physics Research Section A: Accelerators, Spectrometers, Detectors and Associated Equipment 968: 163939. https://doi.org/10.1016/j.nima.2020.163939

Tengattini A., Lenoir N., Andò E. and Viggiani G. (2021) Neutron imaging for geomechanics: A review. Geomechanics for Energy and the Environment 27: 100206. https://doi.org/10.1016/j.gete.2020.100206

van Aarle W., Palenstijn W.J., Cant J., Janssens E., Bleichrodt F., Dabravolski A., De Beenhouwer J., Joost Batenburg K. and Sijbers J. (2016) Fast and flexible X-ray tomography using the ASTRA toolbox. Optics Express 24(22): 25129-25147. https://doi.org/10.1364/OE.24.025129

Vo N.T., Drakopoulos M., Atwood R.C. and Reinhard C. (2014) Reliable method for calculating the center of rotation in parallel-beam tomography. Optics Express 22(16): 19078-19086. https://doi.org/10.1364/OE.22.019078

Vo N.T., Atwood R.C. and Drakopoulos M. (2018) Superior techniques for eliminating ring artifacts in X-ray micro-tomography. Optics Express 26(22): 28396-28412. https://doi.org/10.1364/OE.26.028396

Vo N.T., Atwood R.C. and Drakopoulos M. (2019) Preprocessing techniques for removing artifacts in synchrotron-based tomographic images. In: *Proceedings of SPIE Volume 11113, Developments in X-Ray Tomography XII* (Müller B. and Wang G. (eds)). SPIE. https://doi.org/10.1117/12.2530324

Vontobel P., Lehmann E.H., Hassanein R. and Frei G. (2006) Neutron tomography: Method and applications. Physica B: Condensed Matter 385-386: 475-480. https://doi.org/10.1016/j.physb.2006.05.252

Wadeson N. and Basham M. (2016) Savu: A Python-based, MPI Framework for Simultaneous Processing of Multiple, N-dimensional, Large Tomography Datasets [Preprint]. arXiv:1610.08015

Wennberg O.P., Casini G., Jahanpanah A., Lapponi F., Ineson J., Wall B.G. and Gillespie P. (2013) Deformation bands in chalk, examples from the Shetland Group of the Oseberg Field, North Sea, Norway. Journal of Structural Geology 56: 103-117. http://doi.org/10.1016/j.jsg.2013.09.005

White D.J. and Bolton M.D. (2004) Displacement and strain paths during plane-strain model pile installation in sand. Géotechnique 54(6): 375-397. https://doi.org/10.1680/geot.2004.54.6.375

Figure captions

Figure 1. Example of cylindrical intact chalk sample used.

Figure 2. (a) Schematic diagram of pile installation rig showing NCT and XCT scan zones (note that pile has not yet been installed and that the actuator stem is retracted); (b) photograph of rig mounted on the IMAT tomography stage.

Figure 3. Pile head loads recorded during installation.

Figure 4. XCT reconstructed greyscale-bulk density calibration.

Figure 5. Beam-corrected neutron radiographs (projections) of the chalk sample: (a) in dry condition, (b) after the addition of water (215 minutes after wetting), and (c) after pile installation (750 minutes after wetting). Dotted lines mark data sampling locations (Figure 10). Scalebar units in mm.

Figure 6. Vertical cross-sectional views of reconstructed volumes: (a) NCT before pile installation (dry condition); (b) NCT after pile installation (wet); (c) XCT after pile installation (wet). Scalebar units in mm. Same grey value range used for all images.

Figure 7. Contour maps of volumetric water content distribution derived from neutron radiographs before (215 minutes after wetting) and after pile installation (328 minutes after wetting). Dotted lines marks data sampling location (Figure 9a). Digitally-removed pile shown as blank space.

Figure 8. 3D water saturation (a) and bulk density (b) distribution as derived from NCT and XCT scans, respectively. Dotted lines mark data sampling location (Figure 9b). Digitally removed pile shown as empty space.

Figure 9. Volumetric water content (a) and saturation and bulk density (b) distribution profiles along dotted lines in Figure 7 and Figure 8, respectively.

Figure 10. Flatfield-normalised GV profiles along dotted lines in Figure 5.

Figure 11. (a) Flatfield-normalised GV profiles along horizontal lines in neutron radiographs of (b) dry and (c) wet chalk samples.

Figure 12. (a) XCT and (b) NCT XY slices at a vertical depth of 36.5 mm below the specimen top surface depicting the grey value sampling grid used to correlate the effect of XCT-derived intact chalk dry density on NCT-derived water content measurements, presented in (c).

Accepted manuscript doi:
10.1680/jgeot.21.00318

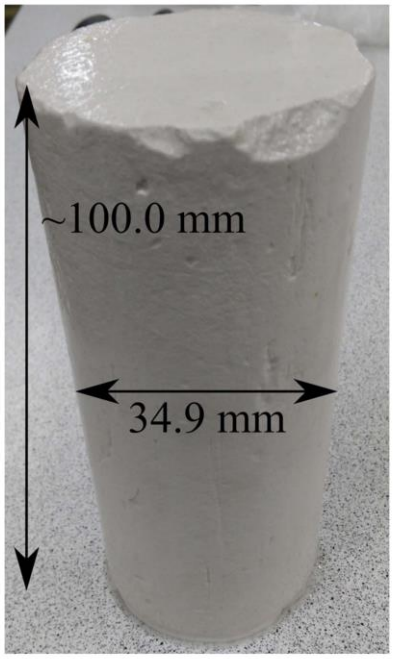

Figure_1

Accepted manuscript doi:
10.1680/jgeot.21.00318

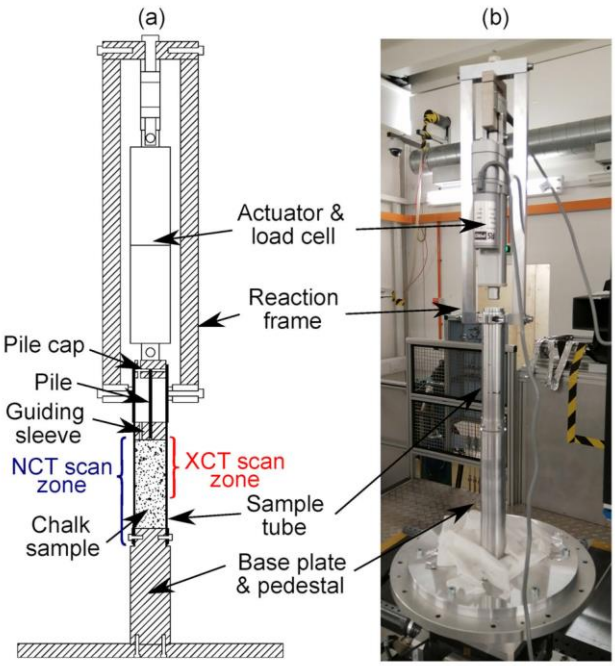

Figure_2

Accepted manuscript doi:
10.1680/jgeot.21.00318

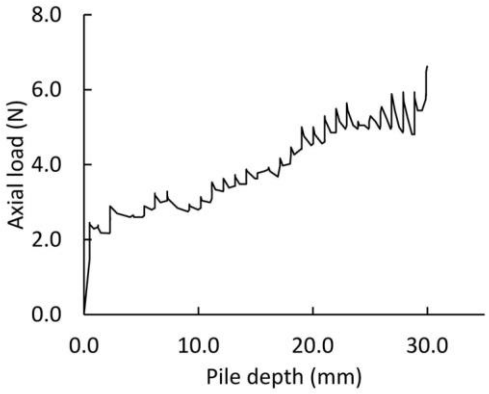

Figure_3

Accepted manuscript doi:
10.1680/jgeot.21.00318

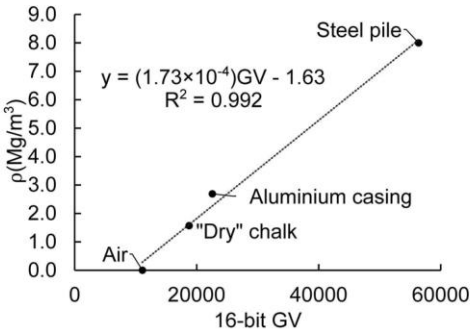

Figure_4

Accepted manuscript doi:
10.1680/jgeot.21.00318

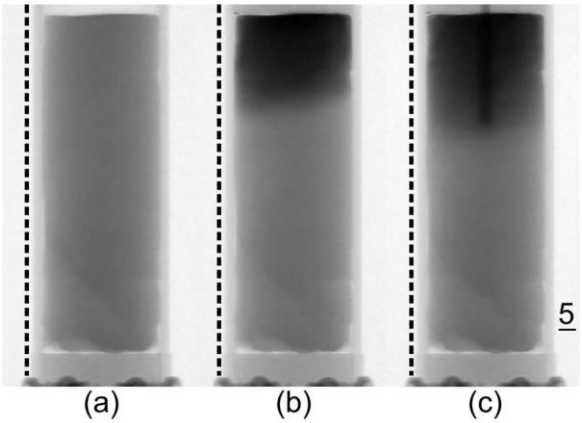

Figure_5

Accepted manuscript doi:
10.1680/jgeot.21.00318

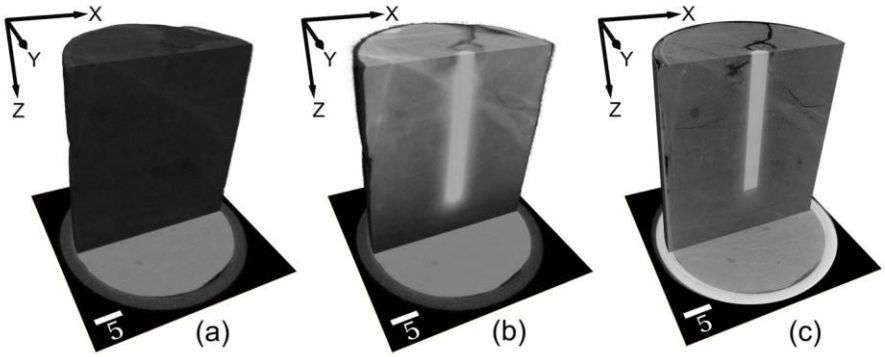

Figure_6

Accepted manuscript doi:
10.1680/jgeot.21.00318

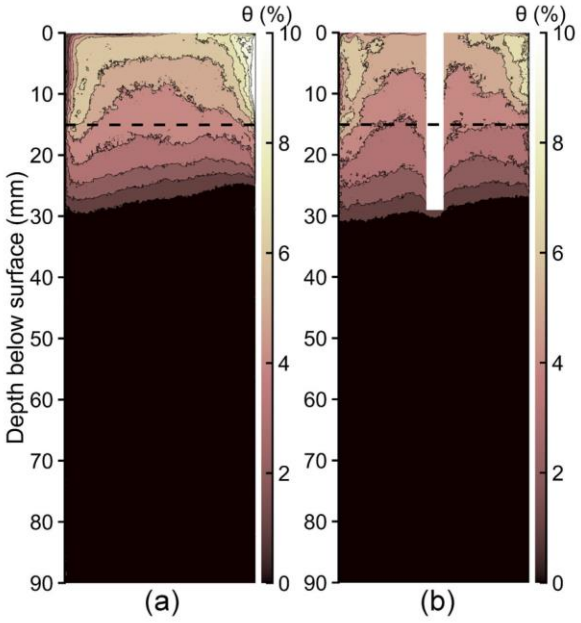

Figure_7

Accepted manuscript doi:
10.1680/jgeot.21.00318

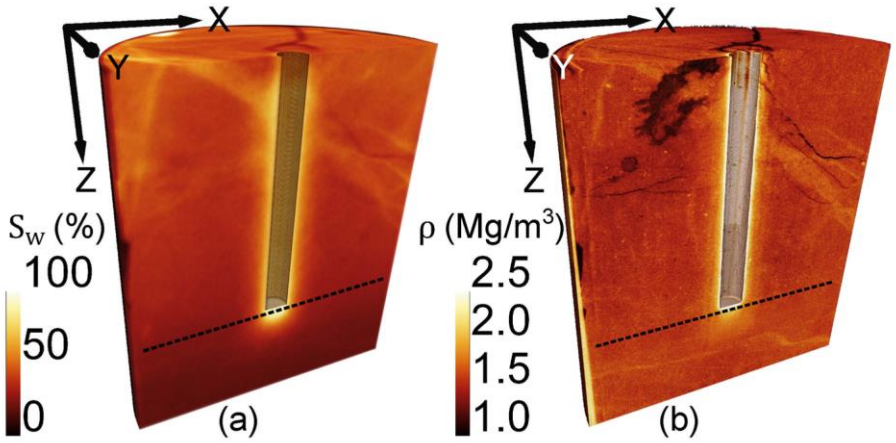

Figure_8

Accepted manuscript doi:
10.1680/jgeot.21.00318

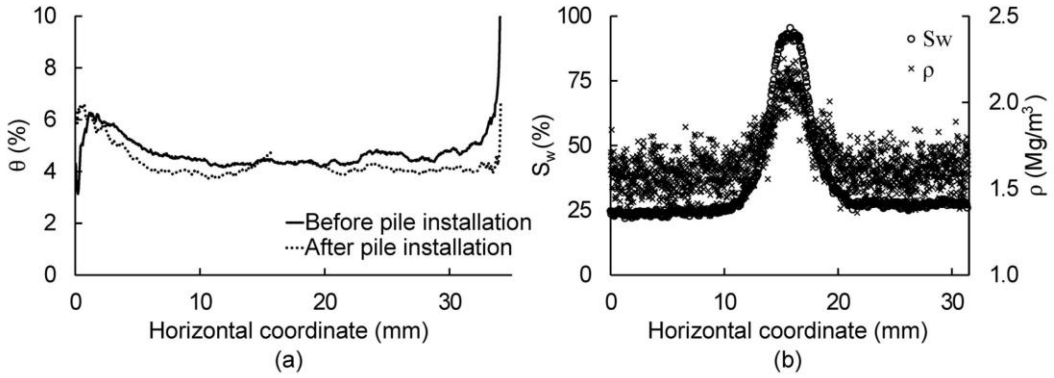

Figure_9

Accepted manuscript doi:
10.1680/jgeot.21.00318

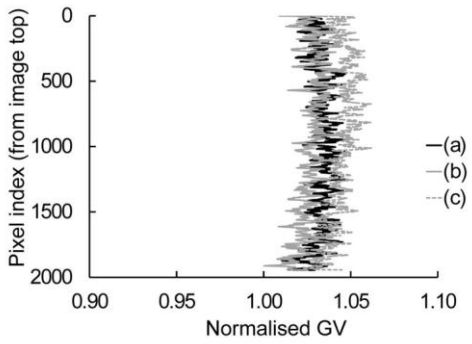

Figure_10

Accepted manuscript doi:
10.1680/jgeot.21.00318

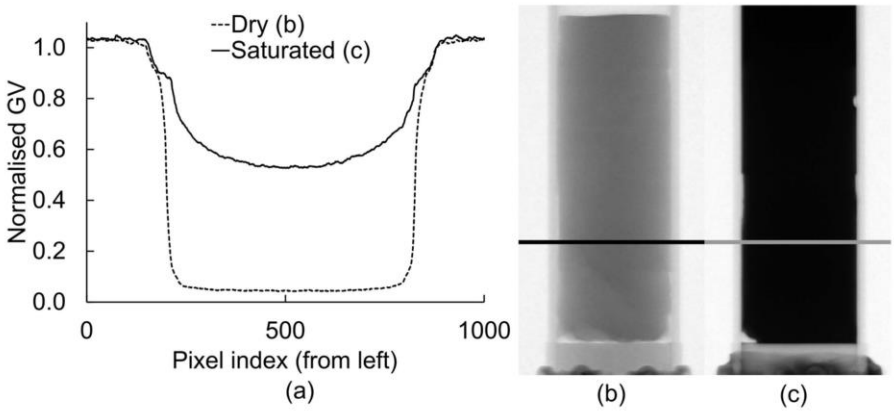

Figure_11

Accepted manuscript doi:
10.1680/jgeot.21.00318

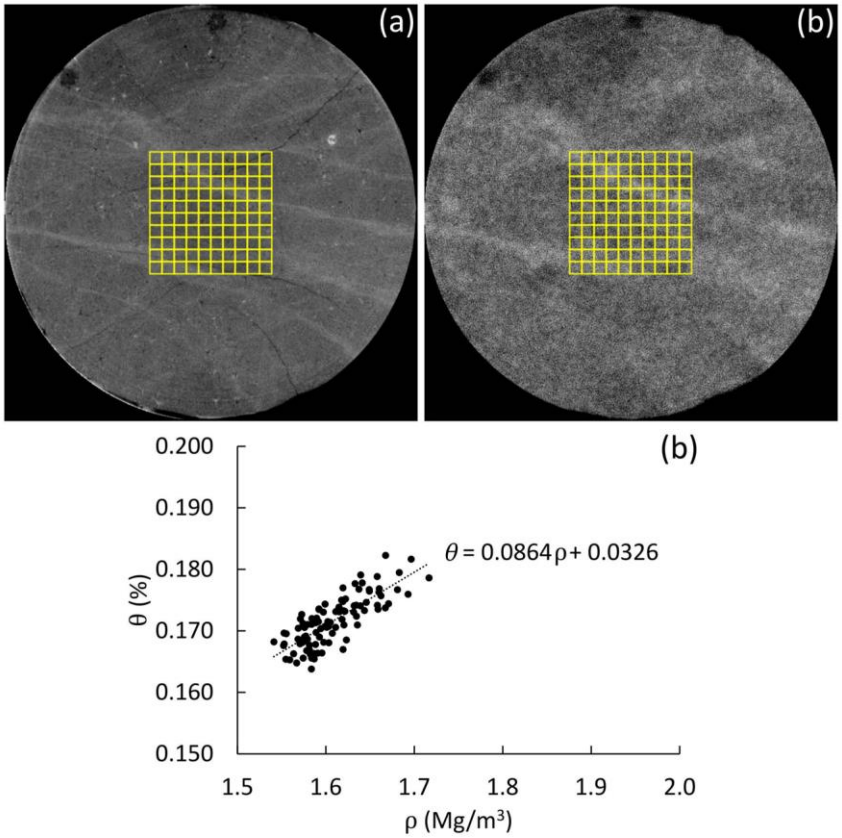

Figure_12